Journal of Crystal Growth 365 (2013) 64–72

Contents lists available at SciVerse ScienceDirect

Journal of Crystal Growth

journal homepage: www.elsevier.com/locate/jcrysgro

Comparison of stirring efficiency of various non-steady magnetic fields during unidirectional solidification of large silicon melts

Natasha Dropka [a,*], Christiane Frank-Rotsch [a], Peter Rudolph [b]

[a] Leibniz-Institute for Crystal Growth (IKZ), Max-Born-Str. 2, 12489 Berlin, Germany
[b] Crystal Technology Consulting (CTC), Helga-Hahnemann-Str. 57, 12529 Schönefeld, Germany

ARTICLE INFO

Article history:
Received 15 August 2012
Received in revised form
4 December 2012
Accepted 5 December 2012
Communicated by A.G. Ostrogorsky
Available online 19 December 2012

Keywords:
A1. Computer simulation
A1. Fluid flows
A1. Magnetic fields
A1. Solidification
B2. Photovoltaic silicon

ABSTRACT

A numerical comparison of various techniques of non-steady magnetic stirring, such as travelling (TMF), rotating (RMF), alternating (AMF) and carousel magnetic fields (CMF), during unidirectional solidification of large rectangular silicon melts of 700 kg was performed. The comparison was focused on the time required to homogenize the distribution of a point wise released tracer in the melt. All studied magnetic fields showed identical magnetic screen and interaction parameter $R_\omega = 80.3$ and $N^{mag} = 7.9 \times 10^{-6}$, respectively. The Lorentz forces were generated in KRISTMAG® heater magnet modules (HMM) positioned at the side or bottom of the silicon melt container. Stirring progress was studied by tracking the formation of the concentration field of the passive tracer in already fully developed melt flow. Results revealed the superiority of the CMF concept independent of the point of injection.

1. Introduction

The current challenges in commercial production of multicrystalline silicon ingots are primarily focused on further improvement of crystal quality and reduction of costs. These goals can be achieved by up scaling of the container dimension, i.e. melt masses and increase of the crystallization rate. However, the problems of high growth velocities are the large amount of generated latent heat, leading to concave bending of the solid-liquid interface, and the enrichment of the diffusion boundary layer in front of the propagating interface. Both effects promote harmful defect formation and redistribution within the crystallizing ingot. Very efficient method to overcome these drawbacks is a forced magnetic convection in which fluid motion in electrically conducting melts is generated by non-steady Lorentz forces [1]. Until today, many technical variations like RMF, TMF and AMF have been tested in laboratory melt growth equipments of relatively small cylindrical geometry. Pros and cons between the methods were balanced. For instance, although strong AMF reduces the thickness of a diffusion boundary layer very effectively, an unfavorable bending of the (Ga, In)Sb interface during vertical Bridgman growth was observed for magnetic induction above 3 mT [2]. Further, the flow controllability at sideward generated TMF was superior relative to RMF [3]. Recently, for the first time a successful application of TMF at the directional solidification of 640 kg (G5) mc-Si ingots has been reported [4]. However, with further increase of ingot mass towards 1000 kg, stirring superiority of sideward produced TMF is questionable. First, to estimate the best field mode for so huge geometry, 3D numeric calculations are of highest importance.

To date, such studies of the electro-magnetic stirring efficiency in large rectangular silicon melts (G4–G5) are still rare [5–8]. Only recently an innovative melt stirring concept by applying carousel magnetic fields (CMF) generated in spiral bottom magnet coils placed around the vertical container axis was proposed [8,9]. However, comparative studies of stirring efficiency between various magnetic fields at such large melt volumes are not yet reported.

Motivated by the lack of results in the literature, this work is devoted to the numerical modeling and comparison of the transient transport phenomena in large rectangular silicon melt of 700 kg under non-steady magnetic fields until a certain degree of homogeneity in the melt with released tracer is achieved.

Lorentz forces were generated by KRISTMAG® HMM [1] positioned close to the outer walls of the rectangular silicon melt container. Depending on the coil positions relative to the melt and to each other, i.e. their arrangement at the side or bottom, but also depending on the current phase shift between coils, TMF, RMF and CMF modes were introduced. Additionally, if coils were supplied with in-phase alternating current (AC), AMFs were generated too.

* Corresponding author. Tel./fax: +49 30 63 92 30 44/03.
E-mail address: natascha.dropka@ikz-berlin.de (N. Dropka).

0022-0248/$ - see front matter © 2012 Elsevier B.V. All rights reserved.
http://dx.doi.org/10.1016/j.jcrysgro.2012.12.009

Nomenclature

B	magnetic induction (T)
Co	Courant number (dimensionless)
Cp	specific heat (J/kg K)
C	tracer concentration (kg/m^3)
D	diffusion coefficient (m^2/s)
E	electric field (V/m)
F	force density (N/m^3)
F	frequency of AC current (Hz)
G	gravity acceleration (m/s^2)
H	magnetic field (A/m)
h	melt height (m)
I	current magnitude (A)
j	current density (A/m^2)
l	melt width (m)
L	characteristic dimension (m)
m	number of HMM coils (dimensionless); melt mass (kg)
n	any integer number (dimensionless)
p	pressure (Pa)
Ra	Rayleigh number (dimensionless)
Re	Reynolds number (dimensionless)
T	temperature (K)
t	time (s)
u	(u_x,u_y,u_z) velocity vector and its components (m/s)
w	tracer mass fraction (kg/kg)
V	melt volume (m^3)
x,y,z	Cartesian coordinates

Greek symbols

α	thermal diffusivity (m^2/s)
β	thermal expansion coefficient (K^{-1})
ϕ	phase shift (°)
λ	thermal conductivity (W/m K)
μ	relative magnetic permeability of material (dimensionless)
μ_0	magnetic permeability of free space (H/m)
ν	kinematic viscosity (m^2/s)
η	dynamic viscosity (Pa s)
σ	electrical conductivity (A/V m)
ρ	density (kg/m^3)

Subscripts

av	average
0	amplitude
buo	buoyancy
L	Lorentz
max	maximal
mag	magnetic
ref	reference
x,y	horizontal coordinate
z	vertical coordinate
∞	perfectly mixed

The comparison of various electro-magnetic stirring concepts was focused on the comparison of their mixing times [10] defined as a time necessary to achieve a 95% degree of homogeneity in the melt, i.e. when the tracer concentration variance in the melt fell below a given value. Such an approach is common in experimental investigations of mixing in chemical stirred tank reactors, where various tracers, such as acid-base-indicators [11,12], electrical conductivity probes [13] and temperature sensors [14] are employed.

Our numerical investigations were aimed to improve understanding of the mixing efficiency during directional solidification of large mc-Si ingots for photovoltaics (PV) and to identify operational electromagnetic parameters crucial for optimization of electro-magnetic stirring process.

2. Model and methodology

The position of heater magnets, their design as well as electromagnetic parameters of supplied AC determined whether TMF (upwards and downwards), RMF, AMF (lateral and longitudinal) or CMF are induced in the melt. For generation of sidewise TMF and AMF, side HMMs consisted of coils arranged upon each other. The phase shift $\Delta\varphi$ among such coils determined the "travelling" direction of the magnetic fields, i.e. $\Delta\varphi > 0^\circ$ for upward directed TMF, $\Delta\varphi < 0^\circ$ for downward directed TMF and $\Delta\varphi = 0^\circ$ for lateral AMF. Alternatively, for generation of RMF, the side HMM coils have to be rearranged longitudinally as "picket fence" design in order to induce azimuthally rotating melt. Such HMM designs for cylindrical crucible geometry have been described more in detail in refs. [15,16]. On the other hand, when the bottom HMM coils are arranged spirally and placed around the vertical axis [8,9], CMF and longitudinal AMF can be induced in the melt. Again, the difference in the phase shift between the coils determined the movement direction, i.e. $\Delta\phi \neq 0^\circ$ for CMF around the vertical axis and $\Delta\phi = 0^\circ$ for longitudinally (upward) acting AMF.

Global magnetic 3D simulations of solidification furnaces were performed for all examined HMM variants and related electromagnetic parameter sets providing Lorentz force density for the local melt simulations.

In order to compare magnetic fields, which can significantly differ in their magnitude, direction and spatial distribution, we set frequency, phase shift and AC magnitude to the values assuring identical magnetic screen parameter R_ω 80.3 (Eq. (1)) and magnetic interaction parameter $N^{mag} = 7.9 \times 10^{-6}$ (Eq. (4)). R_ω value based on frequency $f = 20$ Hz provided a large skin depth δ (Eq. (3)) relative to the melt size L (Eq. (2)). N^{mag} corresponded to the maximal Lorentz force density $\boldsymbol{F}_{L,max} = 1.3 \times \boldsymbol{F}_{buo}$ (buoyancy force given by Eq. (5)) avoiding significant bending of the temperature profile [5]. Phase shift of AC supply in case of CMF was selected using criterion for a constructive interference in $\boldsymbol{F}_L$ spatial distribution, i.e. $\Delta\phi = 360^\circ/im$ with $i = \{0 \ldots n\}$, where m is the number of bottom spirals and n any integer number.

$$R_\omega = 2\left(\frac{L}{\delta}\right)^2 \tag{1}$$

$$L = \sqrt[3]{V} \tag{2}$$

$$\delta = \frac{1}{\sqrt{4\pi 10^{-7}\sigma\pi f}} \tag{3}$$

$$N^{mag} = \frac{\sigma B_0^2}{2\pi\rho f} \tag{4}$$

$$\boldsymbol{F}_{buo} = \rho\beta\boldsymbol{g}\Delta T \tag{5}$$

The global thermal simulation of side arrangements of HMMs with coils positioned upon each other provided thermal boundary conditions for all local melt simulations. Despite that a variation in HMM design causes the change in radiative and conductive heat transfer in the furnace, with a certain effort in a process development, it is possible to adjust the power distribution of the heaters in such a way that very similar temperature distributions at the melt boundaries are obtained. Above proposed approach assured identical thermal environment with axial temperature gradient of $\boldsymbol{G}_T=1\ \mathrm{K\,cm^{-1}}$ for all studied cases and enabled decoupled study of thermal and magnetic influences. Specific details about the global CFD model, mesh geometry and obtained thermal boundary conditions have been already presented in our former paper [8].

In the local 3D simulations we studied the dispersion of an injected tracer in the fully developed melt flow (pseudo steady-state conditions), as in a dye injection experiment. First, we calculated the flow and temperature fields for buoyancy driven silicon melt and used them as starting condition for magnetic driven flows. As the next step we introduced Lorentz forces in the silicon flow and tag the evaluation of the flow and temperature field. At pseudo steady state we froze the flow, released the tracer and, then, solved the mass balance equation of the injected tracer with the same density and viscosity as fluid silicon. Using this approach, the amount of injected tracer and its physical properties did not affect the mixing time.

Numerous papers devoted to the segregation phenomena in stirred containers showed experimentally that the point of injection influences the mixing of tracers [17]. In our numerical experiment we studied the dispersion of tracer injected at two distinct positions, i.e. at melt core and melt bottom corner where we expected extremely delayed convective transport and upper limit of the homogenization time as "worst case". The progress of mixing was monitored by the time evolution of tracer dispersion, i.e. temporal change of maximal tracer mass fraction difference $\Delta w=w_{max}-w_{min}$ in the overall melt volume. The maximal difference Δw reduces its value with a time and finally vanishes if the tracer is perfectly mixed. In this work, the time for complete mixing was defined as the time when average tracer concentration falls below given threshold of $0.05w_\infty$, where w_∞ is the perfectly mixed value calculated as $w_\infty=m_0/V_{melt}$ whereupon w_∞ was set 0.05. The effect of the injection point location was addressed by comparing the values of corresponding mixing times. The maximal value was adopted as a characteristic mixing time for the examined stirring concept.

Considering the liquid silicon as a Newtonian incompressible fluid and neglecting Joule dissipation, the transport phenomenon occurring during magnetically stirred directional solidification of 700 kg mc-silicon melts are governed by the equations of continuity, i.e. Navier Stokes with the Boussinesq approximation, energy balance, species conservation and Maxwell equation together with the Ohms law [Eqs. (6)–(17)].

$$\nabla\bullet\boldsymbol{u}=0 \tag{6}$$

$$\rho\left(\frac{\partial\boldsymbol{u}}{\partial t}+(\boldsymbol{u}\bullet\nabla)\boldsymbol{u}\right)=\rho\boldsymbol{g}-\nabla p+\mu\nabla^2\boldsymbol{u}+\boldsymbol{F_L} \tag{7}$$

$$\rho\boldsymbol{g}=\rho_{ref}\left(1-\beta T_{ref}\right)\boldsymbol{g} \tag{8}$$

$$\rho C_P\left(\frac{\partial T}{\partial t}+(\boldsymbol{u}\bullet\nabla)T\right)=\lambda\nabla^2T \tag{9}$$

$$\frac{\partial C}{\partial t}+(\boldsymbol{u}\bullet\nabla)C)=D\nabla^2C \tag{10}$$

$$\nabla\boldsymbol{H}=\boldsymbol{j} \tag{11}$$

$$\nabla\boldsymbol{E}=-\frac{\partial\boldsymbol{B}}{\partial t} \tag{12}$$

$$\nabla\bullet\boldsymbol{B}=0 \tag{13}$$

$$\nabla\bullet\boldsymbol{E}=0 \tag{14}$$

$$\boldsymbol{j}=\sigma(\boldsymbol{E}+(\boldsymbol{uB}))\approx\sigma\boldsymbol{E} \tag{15}$$

$$\boldsymbol{B}=\mu\mu_0\boldsymbol{H} \tag{16}$$

$$\boldsymbol{F_L}=\boldsymbol{jB} \tag{17}$$

The mesh for local CFD melt simulations consisted of 1.1×10^6 hexagonal mesh elements with refinements at the melt periphery. Boundary conditions for the melt flow were no slip at crucible walls and free slip at the free melt surface. Turbulence was accounted by using k_ω SST model. The time step in transient simulations was adjusted to Courant number $Co\leq1$.

For 3D CFD simulations, we used the commercial finite-volume code ANSYS CFX 13.0. Magnetic 3D simulations were performed using finite elements commercial code ANSYS Emag.

The results were discussed using dimensionless numbers such as Reynolds *Re* Eq. (18) and Rayleigh *Ra* Eq. (19) numbers that give a ratio of inertial to viscous and buoyancy to viscous forces, respectively.

$$Re=\frac{uL\rho}{\eta} \tag{18}$$

$$Ra=GrPr=\frac{\beta g\Delta TL^3}{\nu\alpha} \tag{19}$$

Additionally, we compared mixing time for different stirring configurations with buoyancy time t_{buo} evaluated as a ratio between the path lengths L and volume average velocity in the buoyancy flow $\boldsymbol{u}_{av,buo}$ (Eq. (20)). The buoyancy time is analog to the circulation time necessary for a fluid element to circulate over a reference distance [19].

$$t_{buo}=\frac{L}{\boldsymbol{u}_{av,buo}} \tag{20}$$

3. Results and discussion

3.1. Lorentz force density

The simulated streamlines of Lorentz force density in the molten silicon are shown in Figs. 1 and 2 for upwards and downwards TMFs, lateral and longitudinal AMFs, RMF and CMF.

As mentioned above, we kept constant the maximal magnitude of Lorentz force density and its ratio to buoyancy force density ($\boldsymbol{F}_L=7\mathrm{N/m^3}$; $\boldsymbol{F}_L/\boldsymbol{F}_{buo}=1.3$) in all studied cases by simply adjusting the amplitude of AC. Also the AC frequency was in all cases equal $f=20$ Hz, providing identical penetration depth of $\delta=0.103$ m. Phase shift was set to $\Delta\phi=90^\circ$ for TMFs, AMFs and CMF, since this value in combination with selected frequency $f=20$ Hz provided pronounced inclination of $\boldsymbol{F}_L$ towards the crucible wall. Additionally, in case of CMF with 4 spiral bottom coils $\Delta\phi=90^\circ$ satisfies the criterion for a constructive interference in $\boldsymbol{F}_L$ spatial distribution in order to assure rotational symmetry.

As can be seen from Figs. 1 and 2, the position of the Lorentz forces maximum was located in all cases at the bottom or at the side crucible walls, depending wherefrom magnetic field originated. In case of CMF, one central maximum appeared at the vertical axis of symmetry (Figs. 2 and 3b). In case of AMF with

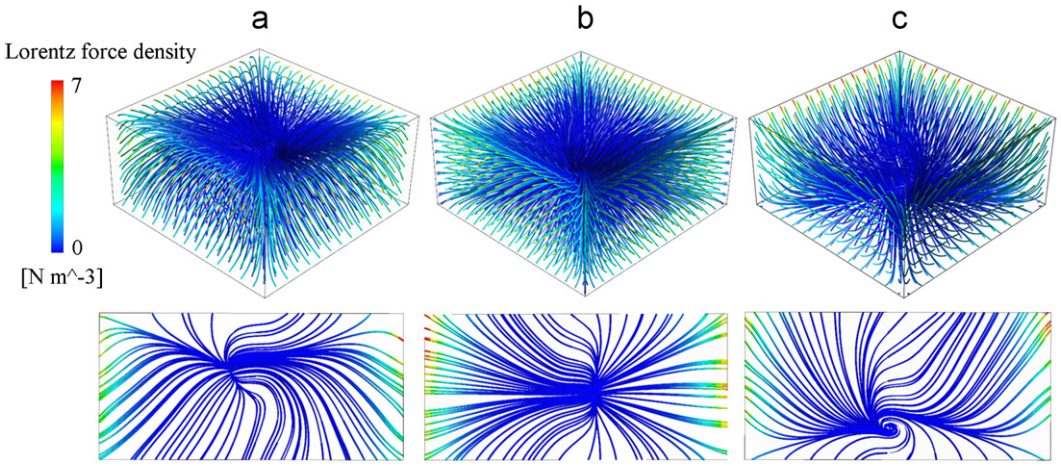

Fig. 1. Lorentz force density streamlines in the silicon melt corresponding to: (a) upwards TMF (side HMMs; $f=20$ Hz; $\Delta\phi=90^\circ$); (b) lateral AMF (side HMMs; $f=20$ Hz; $\Delta\phi=0^\circ$) and (c) downwards TMF (side HMMs; $f=20$ Hz; $\Delta\phi=-90^\circ$): iso view and projection on mid-vertical plane.

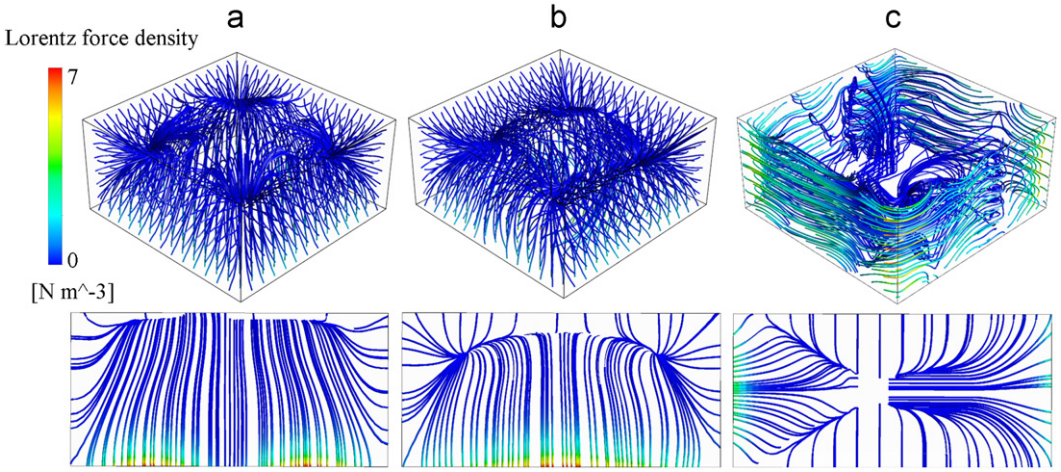

Fig. 2. Lorentz force density streamlines in the silicon melt corresponding to: (a) longitudinal AMF (bottom HMMs; $f=20$ Hz; $\Delta\phi=0^\circ$); (b) CMF (bottom HMMs; $f=20$ Hz; $\Delta\phi=90^\circ$) and (c) RMF (side HMMs; $f=20$ Hz; $\Delta\phi=90^\circ$): iso view and projection on mid-vertical plane and horizontal planes at 25% of the melt height (a), (b) and at 50% of the melt height (c).

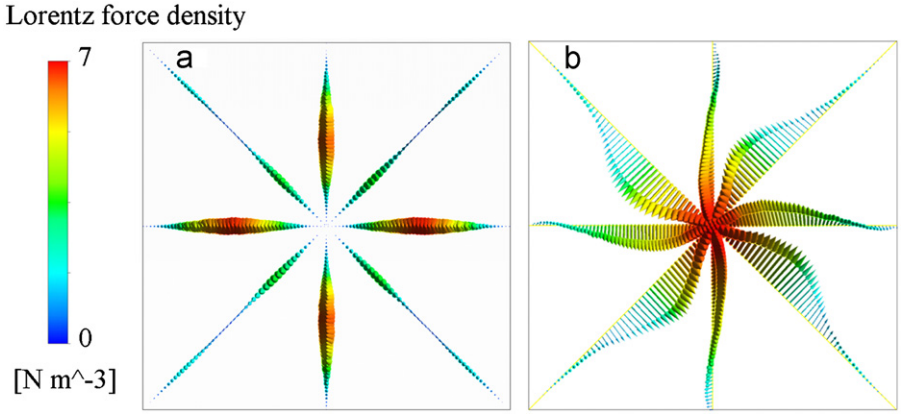

Fig. 3. Lorentz force density vectors in the silicon melt along the characteristic horizontal axis: (a) longitudinal AMF (bottom HMMs; $f=20$ Hz; $\Delta\phi=0^\circ$) and (b) CMF (bottom HMMs; $f=20$ Hz; $\Delta\phi=90^\circ$): top view.

upwards longitudinally directed forces four maxima of $\boldsymbol{F}_L$ being spread along the horizontal melt axes at the melt bottom were observed (Figs. 2 and 3a).

The spatial $\boldsymbol{F}_L$ distribution at upwards TMF is shown in Fig. 1a. Upwards directed $\boldsymbol{F}_L$ streamlines starting from the side walls dominated the distribution. In the upper melt corners the $\boldsymbol{F}_L$ streamlines promptly reverted downwards and finally terminated all together at the core region.

$\boldsymbol{F}_L$ streamlines corresponding to lateral AMF are shown in Fig. 1b. At the middle of the side walls $\boldsymbol{F}_L$ streamlines were directed laterally and terminated in the melt core. Streamlines starting from the corners were aligned with a melt triagonals.

In case of TMF downwards $\boldsymbol{F}_L$ streamlines are shown in Fig. 1c. The obtained distribution proved to be a mirror image of upwards TMF with respect to the mid-horizontal plane.

In Fig. 2a and b the $\boldsymbol{F}_L$ distributions for longitudinal AMF and CMF are depicted. Despite their generally upwards direction their distribution significantly differs in the vicinity of the bottom wall. As in the case of CMF ($\Delta\phi=90^\circ$) the phase shift among the bottom HMM coils induced a revolution of the Lorentz forces around the vertical melt axis and their inclination in the vicinity of the melt bottom where one central maximum emerged (Fig. 3). The smaller the frequency, the stronger the F_L inclination.

The $\boldsymbol{F}_L$ distribution for RMF is given in Fig. 2c. It is dominated by azimuthally time-averaged body force limited to the melt side periphery, having pronounced rotary stirring potential and negligible potential for the motion in axial direction.

Depending on the operational requirements, such as: (i) stirring with the aim to control the impurity distribution and prevent foreign particle inclusions in the crystal and/or (ii) interface shaping, various $\boldsymbol{F}_L$ distributions may be beneficial for the crystal growth. For example, the downwards directed $\boldsymbol{F}_L$ with maximum at the container side walls has a potential to improve the interface morphology and enhance convexity. On the other hand, the upwards directed $\boldsymbol{F}_L$ at the same location may deteriorate the interface shape enhancing concavity. Nevertheless, upwards distribution is favorable for the oxygen transport from the container walls towards the melt free surface, enabling oxygen evaporation in the second step. Azimuthally rotating and lateral $\boldsymbol{F}_L$ distributions may be advantageous for flatting the interface, but not for the bending. The most promising $\boldsymbol{F}_L$ distributions seems to be these originating from the bottom with maximal force located in the diffusion boundary layer in front of the solid/liquid interface and directed upwards, as it the case of CMF and longitudinal AMF. Their particular advantages are potential for depletion of a diffusion boundary layer, i.e. enhancement of the melt velocity without destabilizing the crucible coating, and interface shaping if only one central maximum of $\boldsymbol{F}_L$ distribution exists.

3.2. Flow and temperature fields

In dependency on the mode of used non-steady magnetic field, initial buoyancy flow patterns and temperature fields can markedly change. The temperature distribution at the mid-vertical plane for all studied magnetically driven flows is given in Fig. 4. Deflections of the temperature profile are given in Table 1 in non-dimensional form using Ra number.

No significant temperature changes with respect to the buoyancy case were observed for the flow exposed to lateral AMF (see Fig. 4b). Except slightly positive deflection in the upper melt part the temperature profile remained flat. More pronounced temperature distribution with overall positive deflection, that improves the interface shape towards convexity, was observed at downward TMF (see Fig. 4c), as already was reported elsewhere [1,4,18]. Such slightly convex morphology benefits the growth conditions due to the peripheral rejection of impurities and foreign micro particles. Contrary to that maximal negative deflection relative to buoyancy driven case, leading to concave bending of the interface, is typical for upwards TMF (see Fig. 4a). Longitudinal AMF (see Fig. 4d) showed only negligible improvement in the melt core region but weak negative deflection with four maxima at the melt bottom periphery. A certain disadvantageous negative deflection with maximum at the melt bottom center has been observed when CMF driven flow was applied (Fig. 4e). This result is due to the too strong maximal $\boldsymbol{F}_L$ magnitude generated by the selected set of magnetic parameters. Probably, the definition of characteristic length for R_ω and N^{mag} was unfavorable, however, chosen according to the condition of uniformity compared with all another fields. In our numeric experiment with rectangular form of the silicon melt the ratio between δ and melt size along $\boldsymbol{F}_L$ differed for the sidewise and bottom wise induction. Therefore, these cases may be treated individually, i.e. instead of universal $L=\sqrt[3]{V}$ one can use (i) $L=h/2$ for "bottom" fields and (ii) $L=l/2$ for "side" fields. Such a change in definition of L will consequently impose the change of magnetic parameters in order to preserve the uniform R_ω and N^{mag} values. For practical application at rectangular melts with $h<l$, bottom fields could have higher f and lower B_0 as well as a lower $\boldsymbol{F}_L$ magnitude in comparison with the "side" fields.

Figs. 5 and 6 show the visualized main flow characteristics of the magnetically stirred melts by using velocity streamlines in 2D/3D. As can be seen, the flow structure strongly depends on the $\boldsymbol{F}_L$ force which drives the fluid along and/or out of the region near the crucible wall.

Of course, upwards and downwards directed TMFs (Fig. 5a and c) provoked intensification of the flow first of all at the melt side periphery generating one main slightly non-coaxial vortex and several small vortices in the corners. The center of the main vortex is moving with the melt height. In addition to the axial vortices several vortices with horizontal rotation axis arose in the melt corners giving the flow fully 3D character. Here and along the top and bottom diagonals the maximal velocities were obtained. Such flow asymmetry can be attributed to the distribution of the $\boldsymbol{F}_L$ in the

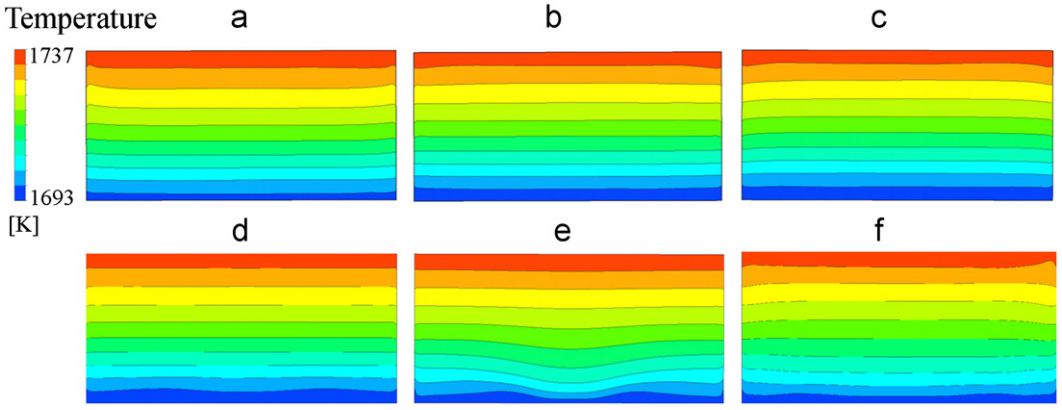

Fig. 4. Snapshots of temperature field at mid-vertical plane for the flow driven by: (a) TMF upward (side HMMs; $f=20$ Hz; $\Delta\phi=90^\circ$); (b) AMF lateral (side HMMs; $f=20$ Hz; $\Delta\phi=0^\circ$); (c) TMF downward (side HMMs; $f=20$ Hz; $\Delta\phi=90^\circ$); (d) AMF longitudinal (bottom HMMs; $f=20$ Hz; $\Delta\phi=0^\circ$); (e) CMF (bottom HMMs; $f=20$ Hz; $\Delta\phi=90^\circ$) and (f) RMF (bottom HMMs; $f=20$ Hz; $\Delta\phi=90^\circ$).

Table 1
Mixing time i.e. time requirements to 95% homogeneous distribution from point wise release of a tracer in the melt and corresponding Re numbers; buoyancy time $t_{buo}=L/\boldsymbol{u}_{av,buo}=468.8$ s.

Driving force	t_{mix}/t_{buo} (dimensionless) bottom corner injection point	t_{mix}/t_{buo} (dimensionless) core injection point	Efficiency rank	Re_{av}	Re_{max}	Ra
CMF	1.89	1.5	1	2.03×10^4	7.24×10^4	2.0085×10^9
RMF	2.82	1.7	2	3.99×10^4	9.56×10^4	2.0087×10^9
TMF up	4.63	4	3	3.79×10^3	3.09×10^4	2.0095×10^9
TMF down	4.99	3.8	4	4.08×10^3	3.09×10^4	2.0097×10^9
AMF lateral	5.04	3.6	5	3.73×10^3	2.87×10^4	2.0097×10^9
AMF longitudinal	7.42	5.1	6	2.76×10^3	2.88×10^4	2.0094×10^9
pure buoyancy	8.3	4.5	7	2.63×10^3	2.69×10^4	2.0096×10^9

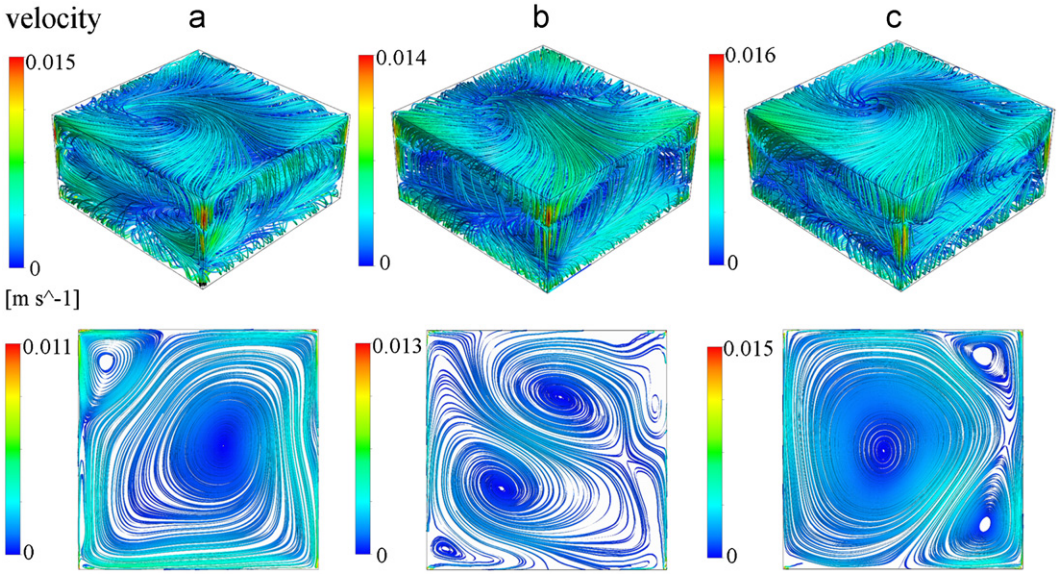

Fig. 5. Snapshots of the velocity streamlines in a silicon melt exposed to: (a) TMF upward ($f=20$ Hz; $\Delta\phi=90^\circ$); (b) AMF lateral ($f=20$ Hz; $\Delta\phi=0^\circ$) and (c) TMF downward ($f=20$ Hz; $\Delta\phi=-90^\circ$): iso view and projection on mid-horizontal plane.

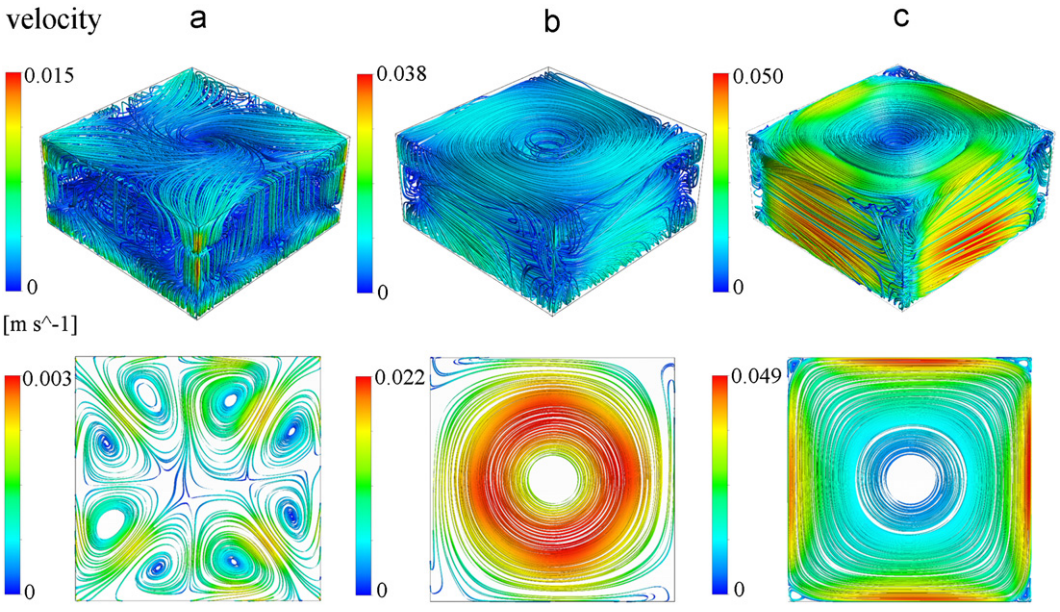

Fig. 6. Snapshots of the velocity streamlines in a silicon melt exposed to: (a) AMF longitudinal ($f=20$ Hz; $\Delta\phi=0^\circ$); (b) CMF ($f=20$ Hz; $\Delta\phi=90^\circ$) and (c) RMF ($f=20$ Hz; $\Delta\phi=90^\circ$): iso view and projection on horizontal plane at 25% of the melt height (a), (b) and at 50% of the melt height (c).

melt. Average and maximal *Re* numbers corresponding with the melt volumes are given in Table 1.

The lateral AMF with its prevailing horizontal $\boldsymbol{F}_L$ triggered the flow pattern towards 3D (Fig. 5b), but now two dominating axial vortices appeared being also typical for buoyancy driven flow with slight asymmetry of the side thermal boundary conditions (BC).

Lorentz forces originated from the bottom, being typical for CMF and longitudinal AMF (Fig. 6a and b), induced strong circulation in the bottom part of the melt. As a whole, CMF increased markedly the average volume melt velocity more than by twice compared to TMFs and lateral AMF. On the other hand, many small axial vortices emerged at the melt bottom periphery in case of longitudinal AMF in comparison to only one pronounced central axial helical vortex in case of CMF. The location of the velocity maximum was shifted from the side and upper melt regions towards the melt bottom.

Finally, RMF generated a strong azimuthal circulation with a triple maximal velocity of other field modes (Fig. 6c). The maximum was located at the side walls and coincided with the maximum of Lorentz forces. One single axial vortex dominated the flow.

The obtained results pointed out that the search for the optimal magnetic field distribution for the melt homogenization cannot be performed independently without considering interface morphology constrains. Such a search is also strongly coupled with the initial "buoyancy" state of the melt, particularly with the initial bending of the temperature distribution, purity of the silicon loading, purity of the gas atmosphere above the melt and chemical/mechanical stability of the crucible Si_3N_4 coating as a possible source of impurities. Depending on the issue and its weighting, the magnetic field distribution can be tailor-made.

Generally, the most promising mode seems to be CMF as it facilitates fluid transport in both azimuthal and meridional directions without destabilization of the crucible coating. However, its magnetic parameters have to be carefully optimized to prevent concave deflection of temperature distribution in the vicinity of the propagating interface and weakening of F_L with the progress of crystallization front due to growing distance between HMM and the melt.

3.3. Concentration field and mixing time

If the tracer was injected in the melt core pure buoyancy will spread its elevated concentration upwards until the free melt surface is reached (Fig. 7a). Afterward the tracer was rejected downwards to the bottom melt region and here distracted in radial direction with very slowing rotation around the central axis of symmetry. After reaching the side walls the propagation switched frontally upwards until the final homogenization point was reached. For the tracer injected in the bottom melt corner (Fig. 7b) the spreading was initially of azimuthal direction around the vertical axis and afterwards pushed slowly upwards. Generally, the total time required for homogenization when starting from the bottom corner was longer relative to the dispersion from the melt core (Table 1). The obtained value of $8.3t_{buo}$ needed for total mixing was in agreement with the experimental observations from the literature of $5–10t_{buo}$ where t_{buo} accounts for the quasi-random paths of the flow [19]. Tracer tracking in magnetic driven flows showed various pathways but always significantly shorter time of total homogenization than the buoyancy flow (Figs. 7 and 8; Table 1). In all studied cases the homogenization time for a bottom corner injection point was longer than for the injection in the melt core. The most efficient stirring was achieved by using CMF, followed by RMF and upwards TMF. CMF exhibited 4.4 times shorter total mixing time relative to the pure buoyancy. The most unfavorable results were achieved by stirring with longitudinal AMF. This outcome can be much better understood if the evolution, location and underlying structure of the segregated regions are further examined.

The spreading of the tracer exposed to CMF was partly mirroring the buoyancy pathway with respect to the horizontal mid plane (Fig. 8a). For the central injection point, the high concentration zone moved first downwards being then rejected

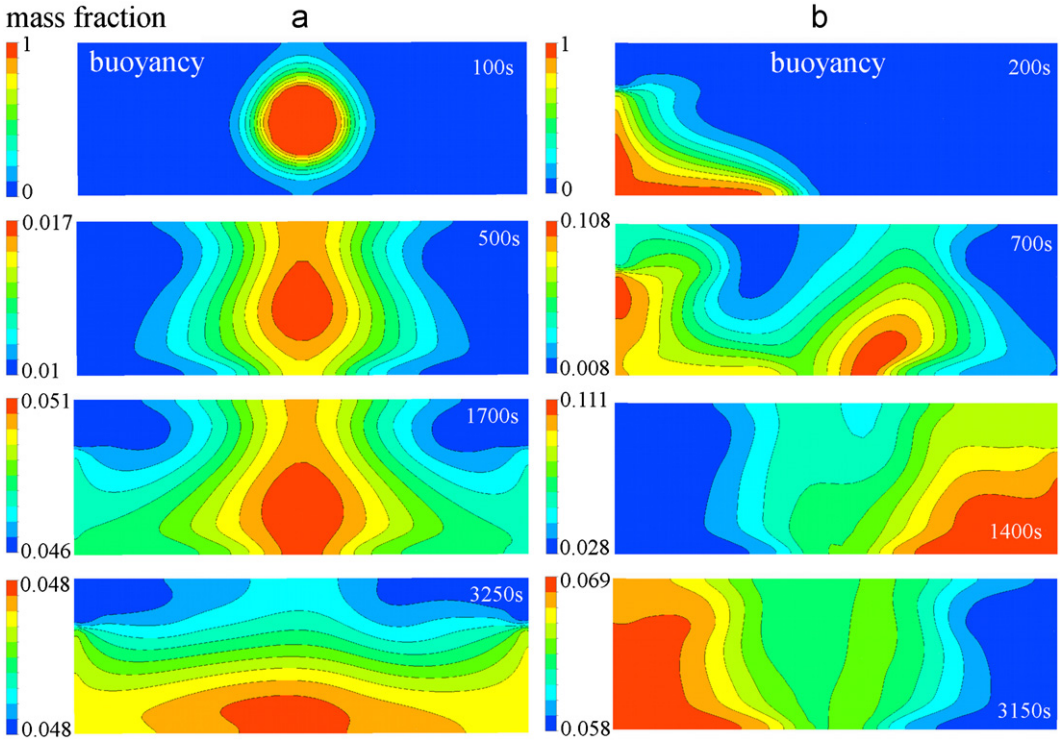

Fig. 7. Temporal tracer concentration profile at diagonal cross section for buoyancy driven flow with injection point at: (a) melt core and (b) melt bottom corner.

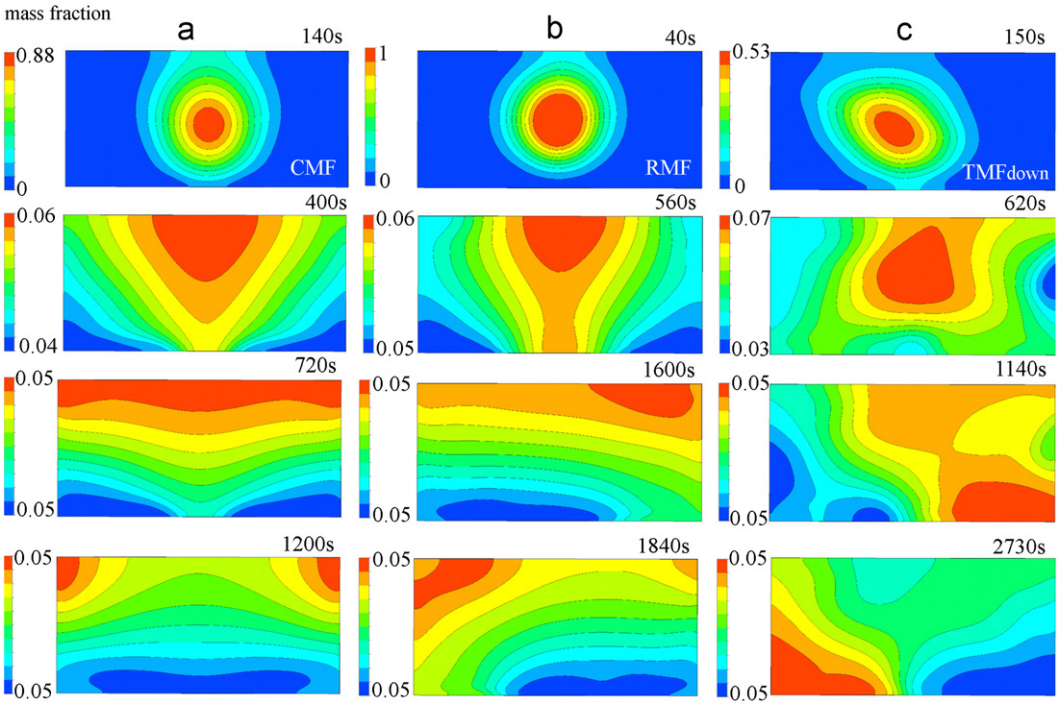

Fig. 8. Temporal tracer concentration profile at mid-vertical plane for stirring by: (a) CMF (f=20 Hz; $\Delta\phi$=90°); (b) RMF (f=20 Hz; $\Delta\phi$=90°) and (c) TMF downward (f=20 Hz; $\Delta\phi$=−90°). Tracer released at the melt core.

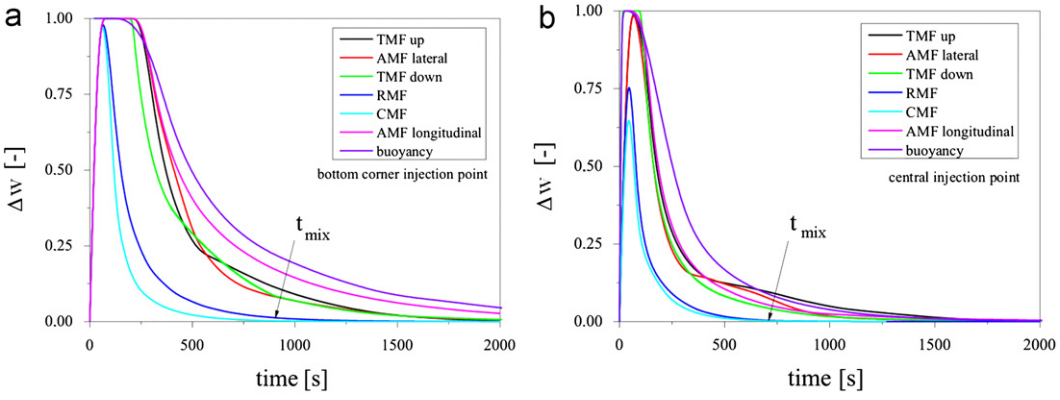

Fig. 9. Time evolution of tracer dispersion, i.e. temporal change of maximal tracer mass fraction difference $\Delta w = w_{max} - w_{min}$ in the overall melt volume for non-steady magnetic stirring and buoyancy driven flows depending on the point of the tracer injection: (a) at the bottom corner and (b) at the melt core.

upwards towards the melt free surface. Once being there, the tracer spread radial and slowly sidewise downwards until the full homogenization was reached. The same is valid for RMF driven flow where additionally the vigorous rotational movement around the central vertical axis was observed (Fig. 8b). Upwards TMF dispersed the tracer in asymmetric way through the melt in both lateral and longitudinal directions with pronounced rotational character but less vigorously than RMF. Downwards TMF with its slightly asymmetric downwards directed $\boldsymbol{F}_L$ was initially pushing the melt downwards along the side walls. Due to the moment conservation, the flow in the melt core was directed opposite that resulted in the upwards transport of the tracer in case of central injection point. After reaching the melt top tracer was rejected sidewise downwards simultaneously rotating around the vertical axis (Fig. 8c). Rotational behavior was not noticed by any AMF driven flow.

Above results showed that the most efficient stirring of silicon melts at the large scale, being of highest importance for improved ingot quality, can be achieved with CMF, RMF and TMF that generate the most intensive circulation, i.e. turbulence (see *Re*, Table 1) in the melt without generation of large stagnant regions (dead zones) where segregation can take place. Additionally, magnetic fields enabling both azimuthal and meridional transport of the species in the melt needed less time for achieving the total homogenization in comparison to the fields with one pronounced transport direction, if started from the identical "buoyancy" thermal and flow distribution. However, the optimal $\boldsymbol{F}_L$ distribution remains the intrinsic property of each set-up, its design and process parameters (Fig. 9).

4. Conclusions

All studied magnetic driven flows in rectangular large-scale crucibles are able to intensify melt circulation up to full homogenization in a shorter time than needed by pure buoyancy. This is of essential advantage for real crystallization processes where effective mixing for reduction of the diffusion boundary layer at

the growing solid-liquid interface and also slightly convex interface bending are required. Additionally, the velocity of the melt proves to be sufficient to carry tracer or any dissolved material into the most remote parts of the crucible. The more turbulent the flow was the better mixing was obtained as has been noticed by comparison of *Re* numbers (Table 1) for various non-steady magnetic fields. The most efficient stirring by considering the mixing time was achieved by CMF, followed by RMF and TMFs. However, final ranking should be performed taking into account the temperature deflection constrains.

Acknowledgments

Part of this work was partially supported by the German Federal State of Berlin in the framework of the "Zukunftsfonds Berlin" and the Technology Foundation Innovation center Berlin (TSB). It was co-financed by the European Union within the European Regional Development Fund (EFRE). Further support was given by the Leibniz Association within the "Pact of Research and Innovation". Fruitful discussions with M. Wünscher are kindly acknowledged.

References

[1] P. Rudolph, Journal of Crystal Growth 310 (2008) 1298–1306.
[2] A. Mitric, T. Duffar, V. Corregidor, L.C. Alves, N.P. Barradas, Journal of Crystal Growth 310 (2008) 1424–1432.
[3] P.A. Nikrityuk, K. Eckert, R. Grundmann, Metallurgical and Materials Transactions B 41 (2010) 94–111.
[4] P. Rudolph et al., Proceedings of the 5th International Workshop on Science and Technology of Crystalline Silicon Solar Cells (CSSC-5), Boston, November 1–3, 2011.
[5] N. Dropka, W. Miller, R. Menzel, U. Rehse, Journal of Crystal Growth 312 (2010) 1407–1410.
[6] N. Dropka, W. Miller, U. Rehse, P. Rudolph, F. Büllesfeld, U. Sahr, O. Klein, D. Reinhardt, Journal of Crystal Growth 318 (2011) 275–279.
[7] C. Tanasie, D. Vizman, J. Friedrich, Journal of Crystal Growth 318 (2011) 293–297.
[8] N. Dropka, Ch. Frank-Rotsch, P. Rudolph, Journal of Crystal Growth 354 (2012) 1–8.
[9] N. Dropka, Ch. Frank-Rotsch, P. Rudolph, R.-P. Lange, U. Rehse, Patent Description DE 10 2010 041 061 A1.
[10] G. Delaplace, J.C. Leuliet, V. Relandeau, Experimental Fluids 28 (2000) 170–182.
[11] K.W. Norwood, A.B. Metzner, AIChE Journal 6 (1960) 432–437.
[12] A.W. Rice, H.L. Toor, F.S. Manning, AIChE Journal 10 (1964) 125–129.
[13] R.D. Biggs, AIChE Journal 9 (1963) 636–640.
[14] B. Mayr, P. Horvat, A. Moser, Bioprocess Engineering 8 (1992) 137–143.
[15] K. Hoshikawa, H. Kohda, H. Hirata, H. Nakanishi, Japanese Journal of Applied Physics 19 (1980) 33–36.
[16] E.M. Hull, I.B.M. Technical, Disclosure Bulletin 23 (1980) 2756–2757.
[17] D.J. Lamberto, M.M. Alvarez, F.J. Muzzio, Chemical Engineering Science 54 (1999) 919–942.
[18] N. Dropka, Ch. Frank-Rotsch, W. Miller, P. Rudolph, Journal of Crystal Growth 338 (2012) 208–213.
[19] A.W. Patwardhan, J.B. Joshi, Chemical Engineering Science 38 (1999) 3131–3143.